Journal of Building Engineering 98 (2024) 111100

Contents lists available at ScienceDirect

Journal of Building Engineering

journal homepage: www.elsevier.com/locate/jobe

Fire resistance of 3D printed ultra-high performance concrete panels

Arun R. Arunothayan *, Akilesh Ramesh, Jay G. Sanjayan

Center for Sustainable Infrastructure and Digital Construction, Swinburne University of Technology, Hawthorn, VIC, Australia

ARTICLE INFO

Keywords:
3D concrete printing
Fire resistance
Heat transfer
Interlayers
UHPFRC

ABSTRACT

Ultra-high performance fiber-reinforced concrete (UHPFRC) is highly suitable for 3D concrete printing (3DCP) due to its high flexural strength, thereby reducing the need for reinforcements. However, UHPFRC is susceptible to spalling under exposure to fire, limiting its application as structural members. In this paper, the effect of 3D printing process on the fire behavior of UHPFRC is studied, benchmarking against mold-cast panels. The insulation, integrity, and structural adequacy of the panels are investigated using the heat transfer mechanisms, failure modes, and the post-fire compressive strength of the panels, respectively. The presence of interlayers reduced the spalling of UHPFRC under fire and improved the structural integrity of 3D printed specimens compared to mold-cast specimens. Further, the addition of 0.5 % polypropylene (PP) fibers eliminated the interlayer delamination and spalling in 3D printed UHPFRC panels. Similarly, 3D printed panels showed improved structural adequacy than mold-cast specimens. The residual compressive strength of 3D printed UHPFRC panels after being exposed to fire was observed to be above 50 % of the initial mean compressive strength. However, the insulation property of 3D printed panels was reduced compared to that of the mold-cast counterparts due to the high rate of heat transfer via the porous interlayers. The addition of PP fibers improved the insulation resistance of the interlayer region and surface of the 3D printed panels. The strength anisotropy of the 3D printed UHPFRC reduced significantly following the fire exposure. Further, the thermal bowing of 3D printed panels was higher with an increased dosage of PP fibers due to the increase in the thermal strain of UHPFRC. Therefore, adequate care must be given in the design of 3D printed structures for potential fire resistant wall, slab, and façade elements.

1. Introduction

3D concrete printing (3DCP) is an additive manufacturing technology that enables the production of concrete elements with complex geometries by eliminating the use of formworks. The current progress of 3DCP is hampered by the limited material capabilities of printable concretes and reinforcing methods [1–3]. The current state-of-the-art printable concrete composites cannot print the architecturally intricate shapes that 3DCP technology promises. The incorporation of steel reinforcement poses a practical challenge for the operations of 3DCP [4–6]. To address these problems, the authors previously investigated the use of ultra-high performance fiber-reinforced concrete (UHPFRC) for 3DCP applications [7,8]. The UHPFRC composites possess high compressive strength,

* Corresponding author.
E-mail address: rarunothayan@swin.edu.au (A.R. Arunothayan).

https://doi.org/10.1016/j.jobe.2024.111100
Received 17 July 2024; Received in revised form 5 October 2024; Accepted 17 October 2024
Available online 18 October 2024
2352-7102/

List of abbreviations:

3DCP	Three-Dimensional Concrete Printing
UHPFRC	Ultra-High Performance Fiber-Reinforced Concrete
FRL	Fire Resistance Level
T_O	Initial atmospheric temperature
T	Furnace temperature
t	Time
PP	Polypropylene Fiber
HRWRA	High Range Water Reducing Agent
VMA	Viscosity Modifying Agent
I	Anisotropy Index
fc_{MC}	Mean compressive strength
$\varnothing$	Curvature of the bowing effect
ϵ	Thermal strain
ϵ_{cr}	Tensile cracking strain

enabling size efficiency to print concrete members with slender cross-sections. Moreover, the addition of short fibers provides high flexural strength and fracture toughness, thus reducing the reliance on conventional steel reinforcements. The material properties of 3D printable UHPFRC such as mix consistencies, rheological characterization, fiber dispersion and alignment and rapid hardening are notoriously difficult to control and pause significant challenges to industry adoption. A detailed discussion on these challenges is provided by the authors and other researchers elsewhere [9–12].

Despite their superior mechanical properties, UHPFRC composites are generally vulnerable to accidental fire due to their low permeability, which leads to spalling and degradation [13,14]. Two mechanisms that cause the spalling are (1) build-up of pore pressure and (2) restrained thermal expansion [15]. The use of dense particle packing techniques and the elimination of coarse aggregates in UHPFRC mixtures lead to the formation of ultra-dense microstructure. Hence, the porosity of UHPFRC is significantly lower than the normal strength concretes [16]. When the concrete temperature increases during a fire, the moisture in the concrete vaporizes and attempts to escape. In normal-strength concrete elements, the vapor can escape comparatively easily via the pores without causing significant damage to the material. However, the low porosity in UHPFRC elements restricts the escape passages of the vapor, which increases the vapor pressure inside the concrete elements. When this vapor pressure build-up increases beyond the tensile capacity of UHPFRC, explosive spalling occurs [17–19]. Previous studies indicated that lowering the moisture content of UHPFRC specimens below 0.95 % reduces the vapor pressure, thereby preventing spalling [20]. In addition, spalling may occur at very high heating rates due to excessive thermal stresses generated by rapid heating. During rapid heating, compressive stresses form near the exposed surfaces of the concrete while tensile stresses form at surfaces farther from the heat source. The restrained thermal expansion can cause spalling when the thermal stresses exceed the concrete strength capacities [15,21]. This spalling is rarely observed in UHPFRC specimens due to high thermal conduction and ultra-high strength profiles. However, this form of spalling can become dominant when loading or prestress is applied during the fire [21]. UHPFRC column specimens subjected to eccentric loading showed excessive spalling induced by the additional stresses and reduced fire resistance [22]. Further, explosive spalling was observed for UHPFRC specimens subjected to simultaneous fire exposure and impact loading [23].

The fire response of concrete elements is evaluated based on fire resistance level (FRL) criteria according to ISO 834–1:1991 [24] or AS 1530.4:2014 [25]. The FRL of the concrete element is based on its structural adequacy, integrity, and insulation following a fire hazard event. Structural adequacy is the ability to maintain stability and load-bearing capabilities during a fire hazard. Preventing the development of cracks and fissures and thereby limiting the spread of fire is characterized as the integrity of the structure. Insulation is defined as the ability to control the rate of transfer of heat from the fire-exposed surface to the unexposed surface. These three responses are measured in time (i.e., time taken for the prescribed thresholds to occur), and the FRL of a structural element is given in a format of adequacy/integrity/insulation. For example, an FRL of 90/60/30 indicates structural adequacy for 90 min, integrity for 60 min, and insulation for 30 min.

To investigate a concrete element for FRL, fire tests are conducted based on the standard time versus temperature fire curve [24]. The ISO 834 standard fire curve was presented in Equation (1).

$$T - T_O = 345 \log_{10}(8t + 1) \tag{1}$$

where t is the time from the beginning of the fire test in minutes, T_O is the initial atmospheric temperature and T is the furnace temperature at time t. The AS 1530.4:2014 [26] for the fire resistance follows the same standard fire curve, with the exception that T_O is constant and equals 20 °C.

Various fire tests were conducted and reported on the fire resistance of normal strength and high strength concrete elements. The concrete with aging and exposure to fire necessitates additional fire safety protection depending on the risks associated with concrete spalling [27]. The use of polymeric fibers, especially polypropylene (PP) fibers, improves the fire resistance of these concrete elements, thereby preventing spalling failures [18,19,28,29]. For instance, as the concrete temperature increases during a fire, the PP fibers melt in the range of 160–180 °C and create additional escape passages for vapor to escape, thereby reducing the vulnerability of the concrete elements to the spalling failure. However, there are only limited studies conducted to evaluate the fire resistance of UHPFRC elements. In a recent review article, Zhu et al. [30] recommended the need for more large-scale fire tests on UHPC structures to understand the experimental phenomenon in detail. The available fire experiments on UHPFRC elements also provide contrasting outcomes in terms of the efficiency of hybrid fiber systems in reducing the explosive spalling behavior of UHPFRC. Recently, Li et al. [22] tested five UHPFRC columns with and without eccentric loading and concluded the beneficial effects of PP fibers in preventing spalling failures. Lee et al. [31] tested two full-scale UHPFRC columns subjected to ISO 834 standard fie curve and reported minor spalling when a hybrid fiber system of PP fibers, nylon fibers, and steel fibers was used. Kahanji et al. [32] tested large-scale UHPFRC beams under the standard fire curve with a hybrid fiber system of 2 % volume fraction of steel fibers and 0.5 % volume fraction of PP fibers and observed no spalling in the specimens. On the contrary, Choe et al. [33] tested UHPFRC columns with a similar hybrid fiber system under the same standard fire curve and observed severe spalling with a 26 % reduction in the cross-section area. All the experiments above were conducted to imitate the fire on beam and column elements for which the heating was applied from all directions. However, few studies have explored the fire resistance of UHPFRC slab/wall/façade elements where the heating occurs on one side (exposed face) [26]. The structural responses to heating on one side can be different to heating from all sides and warrant further investigations [34,35]. Therefore, further research is needed to understand the fire response of UHPFRC elements with different fiber systems under one-sided heating.

Further, studies on the fire performance of 3D printed elements are also very limited. Cicione et al. [36] conducted an experimental study on the fire behavior of 3D printed specimens and mold-cast specimens made of high-strength concrete. They showed that the failure of 3D printed specimens occurred predominantly at the interlayer, indicating the vulnerability of the interlayers to fire. In addition, the undulating surfaces of 3D printed specimens influenced the heat transfer at the interlayers. Subsequently, Sunthar-alingam et al. [37,38] developed finite element models to numerically analyze the fire performance of 3D printed concrete walls under standard fire conditions and concluded that the 3D printed concrete walls were prone to insulation failure compared to those of mold-cast concrete wall elements. However, the analyses were developed with predetermined microstructure void systems and thermal properties of the concrete mixture, which imitate normal strength and high strength concretes. Further, 3D printed wall el-ements with cavities showed lower fire performance and requires additional insulation materials [38]. The addition of PP fibers and face mask fibers reduces the thermal conductivity of 3D printed specimens resulting in better insulation properties [39]. Further, the influence of fire on the permeability, Young's modulus and fire rating of 3D printed structures need more investigation. The available literature lacks full-scale experimental fire tests of 3D printed concrete elements, particularly 3D printed UHPFRC elements which are more vulnerable to fire than normal concrete. Hence, the fire performance and the spalling behavior of 3D printed UHPFRC panels exposed to different fire scenarios need to be investigated. Unlike mold-cast concrete, the effect of interlayers on the heat transfer and spalling during fire needs detailed investigation for 3D printed UHPFRC elements.

Thus, this study evaluates the fire performance of lightweight panel members 3D printed using UHPFRC with different hybrid fiber systems. The large-scale fire testing conducted in this study evaluated the FRL of 3D printed UHPFRC panels and compared them to their mold-cast counterparts. The 3D printed and mold-cast UHPFRC panels were subjected to ISO 834 standard fire curve test for up to 60 min. The structural adequacy, integrity, and insulation of the 3D printed and mold-cast panel members were investigated. The effects of PP fiber content on the spalling behavior of 3D printed and mold-cast UHPFRC specimens were also discussed.

2. Materials

The development of 3D printable UHPFRC mixtures and their properties were previously discussed by the authors elsewhere [6–8, 40]. The binder comprised 70 % ordinary Portland cement (OPC) and 30 % silica fume (SF) by mass. Three types of sieve-graded silica sands, categorized according to their particle size distributions, were used at a 1:1 binder-to-sand mass ratio. The water-to-binder mass ratio was 0.16. A polycarboxylate ether-based high-range water-reducing admixture (HRWRA) was used in solution form to control the workability. To facilitate a smooth printing process, nano clay (in the form of a highly purified hydrous magnesium aluminosilicate) was used as the viscosity modifying admixture (VMA). Steel and PP fibers were used to reinforce the matrix. The properties of these fibers are given in Table 1.

Mixture formulations were developed with different fiber combinations, as shown in Table 2. The use of polymeric fibers reduced the flowability of the mixture. To compensate for the loss of flowability, the dosage of HRWRA was slightly increased. In addition, VMA content was also reduced to facilitate the printability of the mixtures. The HRWRA and VMA contents of all mixture formulations are given in Table 2 as a percentage of binder mass.

Table 1
Properties of the fibers.

Type	Length (mm)	Diameter (μm)	Tensile strength (MPa)	Density (kg/m^3)	Melting point (°C)
Steel fiber	6	200	2500	7850	1370–1540
PP[a] fiber	6	18	557	910	150–160

[a] Note: PP = Polypropylene Fibers.

Table 2
Mixture designs investigated in the study.

Mix	Steel	PP	OPC	SF	Sands	Water	HRWRA	VMA
S1-P.25	1 %	0.25 %	0.7	0.3	1	0.16	0.01	0.003
S1-P.5	1 %	0.5 %					0.01	0.003
S1-P1	1 %	1 %					0.012	0.002
S1-P1.5	1 %	1.5 %					0.015	0.002
S1-P2	1 %	2 %					0.015	0.002
S0-P2	–	2 %					0.015	0.002

Note: Values of fiber content are volume fraction of the mixture; the rest of the values are a mass fraction of the total binder mass.
PP = Polypropylene fiber; SF = Condensed Silica Fume; HRWRA = High Range Water Reducing Admixture (Superplasticizer); VMA = Viscosity Modifying Agent.

3. Experiments

3.1. Printer setup

A steel frame gantry-type 3D printer with an effective printable workspace of 1.8 m (L) × 1.6 m (W) × 1.8 m (H) was used for this study. An augur-type extruder was mounted to the actuator of the gantry system. A customized computer program controlled the linear axes (X, Y, and Z) movements of the extruder over the printing platform. A steel plate was connected diagonally to the extruder inlet to ease the material feeding process. The outlet of the extruder was attached to a detachable circular nozzle. The gantry printer and the augur-type extruder are shown in Fig. 1.

3.2. Specimen preparation

A 60 L capacity planetary mixer was used to prepare the fresh mixture. First, the dry materials were mixed at low speed for 3 min. Then, 75 % of the mixed water was gradually added and mixed for 5 min. The remaining water was mixed with HRWRA and added gradually to the mixture as proposed previously by Wille et al. [41]. The mixing was continued until the desired mixture rheology was achieved. The steel fibers were then added to the mixture gradually and mixed for an additional 6 min at low speed. Then, the polypropylene fibers were added to the mixture and the mixing was continued for another 3 min at low speed, followed by three further minutes at high speed. Fiber dispersion in the mixture was checked by visual inspection. In the final step, nano clay was added to tailor the rheology of the mixtures to suit the printability requirements. A similar methodology was adopted for mixing by the authors in their previous works [40,42,43].

Flow table tests accordance with ASTM C1437 [44] was conducted to measure the workability of the fresh mixtures. Two orthogonal diameters of the mixture flow were recorded before and after the drops of the flow table.

The rheological behavior and the buildability analysis of the base UHPFRC mixture were previously studied in detail by the authors [43]. Similar rheology characterization was difficult to carry out to determine the printability and buildability of these mixture formulations with different polymeric fiber combinations due to the interlocking effect of the polymer fibers distorting the measurement accuracies. Therefore, a detailed discussion on the rheological characterization was not included in the paper.

Panel sections with a length of 1000 mm and a height of 230 mm were 3D printed, as shown in Fig. 2(a). Each panel section is made of a single filament, having a width of 40 mm and a height of 10 mm (i.e., each panel consists of 23 layers). The extrusion rate was adjusted by controlling the rotation speed of the augur so that the width of the extruded filament was equal to the nozzle diameter. The

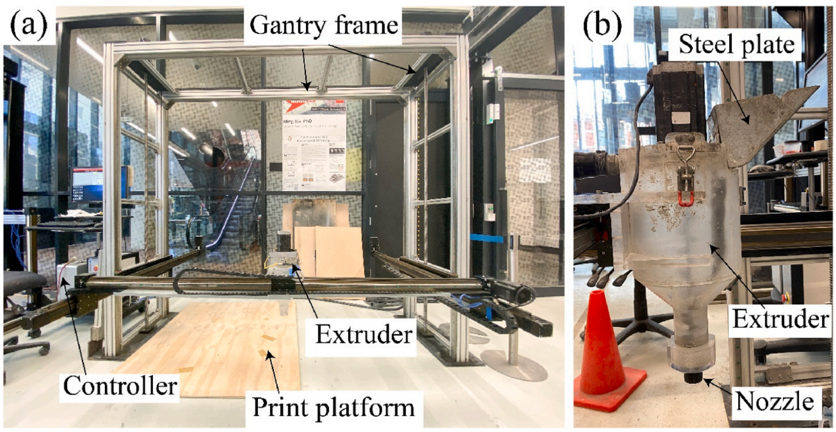

Fig. 1. (a) 3D printer used in the study (b) Extruder and nozzle.

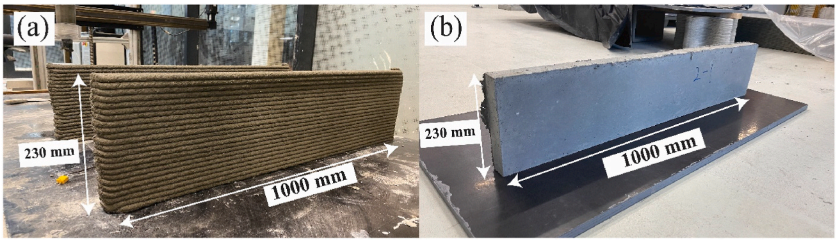

Fig. 2. (a) 3D printed panel specimens (b) Mold-cast panel specimens.

printer was programmed to move up in 10 mm intervals in conjunction with the layer height of the sections. The printing speed was 30 mm/s. At the end of 3D printing, the specimens were covered with plastic sheets to reduce excessive evaporation. For comparison purposes, panels with similar cross-sections were mold-cast in the meantime, as shown in Fig. 2(b). The fresh mixture was gradually poured into custom-made molds and homogeneously dispersed using a portable vibrator. The mold-cast specimens were then covered with plastic sheets for 24 h and demolded afterward. The specimens were then cured for 28 days in room temperature before the fire tests.

3.3. Furnace set up

Fig. 3 presents the furnace used in the study. The furnace was set up to carry out standard time-temperature fire tests by exposing one face of the panels. The furnace opening was 1.9 m long and 1 m wide. The furnace body contains steel shells of a 5 mm rolled plate with 5 mm top and bottom plates stiffened with vertical rectangular hollow sections. The furnace was insulated using stack-boned ceramic fiber with a density of 128 kg/m^3, which was compressed to 160 kg/m^3. The insulation was attached to the furnace body by stainless steel pins welded to the body. The furnace was powered by a single controller up to 125 A of three-phase electricity. The controller was connected to three gauges, which provide real-time records of the internal furnace temperature. More details about the furnace setup can be found in Negahban et al. [45].

The panel specimens were stacked one upon another, exposing one side to the furnace heat. The other side was exposed to room temperature (20 ± 3 °C). The ceramic fiber was placed in between the stacking of panels for insulation. The panels were firmly pressed to the furnace at both edges using steel rods and held in position by C-track connectors. Three mineral-insulated metal sheathed (MIMS) thermocouples having an outer diameter of 3 mm were mounted near the exposed surface of the specimens. These MIMS thermocouples were located at the top, middle, and bottom of the furnace body and denoted as F1, F2, and F3, respectively. Type K thermocouples, each containing a 12 mm diameter copper disk connected to the wire by a silver soldering joint and covered with 30 mm × 30 mm × 3 mm organic insulation pads, were attached to the unexposed surface of the mold-cast and 3D printed specimens using high-temperature resistant epoxy putty. Additionally, thermocouples were installed at the unexposed interlayer zone in 3D printed specimens.

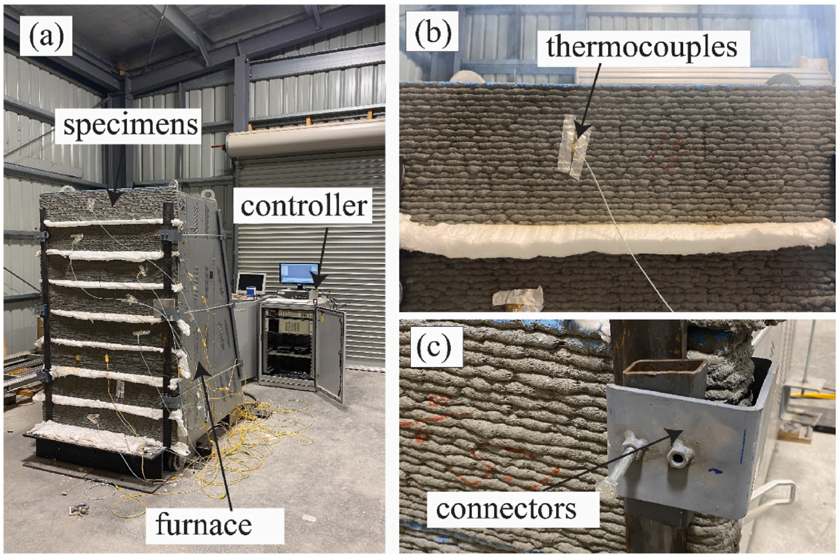

Fig. 3. (a) Furnace set up (b) Thermocouples were attached to the unexposed surface of the panels (c) Connectors were used to hold the panels in position.

The furnace temperature was set to follow the standard fire curve according to ISO 834 [24]. The experiment was conducted for 60 min for panels containing S1-P1, S1-P1.5, S1-P2, and S0-P2 mixtures. The experiment was prematurely terminated after 25 min for S1-P.25 and S1-P.5 mixtures due to explosive spalling. At the end of the tests, the specimens were allowed to cool down to room temperature without disturbance for 24 h. Fig. 4 shows the reference ISO 834 [24] standard fire curve, and the readings detected in F1, F2, and F3 thermocouples.

The measurements from the MIMS thermocouples showed close matching with the standard fire curve. No significant difference was observed between the MIMS thermocouple readings, indicating uniform temperature across the furnace. This shows that all panel members reached comparable temperatures on their exposed surfaces during the experiment. The initial temperature of these specimens was measured before the commencement of the fire test on the unexposed surfaces. The specimens were deemed to have failed in the insulation-criteria if any part of the unexposed surface of the specimen exceeded the initial temperature by 180 °C [46]. The thermal bowing in the panels was recorded by measuring the bending of the panels after the cooling-off period.

3.4. Moisture content

To measure the moisture content at the time of testing, an additional set of mold-cast and 3D printed panels were prepared for each mixture and cured under the same conditions. On the testing day, these panels were weighed, transferred into an oven, and dried at 110 °C. After that, the mass of the panels was measured at 24-h intervals until the change in mass became insignificant. The total mass loss was attributed to moisture loss due to drying.

3.5. Structural adequacy

To measure the structural adequacy of the panels following the fire test, the mold-cast and 3D printed panels were allowed to cool down for 24 h and then removed from the furnace. After that, six cubic specimens from the mold-cast panels and eighteen cubic specimens from the 3D printed panels were cut separately. All sides of the cubic specimens were then ground flat. Then, these specimens were tested for compressive strength at a load rate of 20 MPa/min. The 3D printed specimens were tested in all three directions to investigate the anisotropic behavior of the printing process. The directions are denoted in the following manner, as shown in Fig. 5: 3DP-X – parallel to the printing direction; 3DP-Y – lateral direction in which the material is free to expand while printing; and 3DP-Z – the vertical direction in which the layers are printed one above the other. Six specimens were tested in each loading direction. The anisotropy index (I) is calculated at different target temperatures using Equation (2) [47].

$$I = \sqrt{(fc_X - fc_{MC})^2 + (fc_Y - fc_{MC})^2 + (fc_Z - fc_{MC})^2} \Big/ fc_{MC} \tag{2}$$

where fc_X, fc_Y, fc_Z are the mean compressive strength values of the 3D printed cubic specimens in X, Y, Z directions respectively. fc_{MC} is the mean compressive strength value of the mold-cast cubic specimens of the same mixture [47].

4. Results and discussion

4.1. Workability

The flow (average spread diameter) of the fresh mixtures is presented in Fig. 6. All fresh mixtures had almost zero slump before the

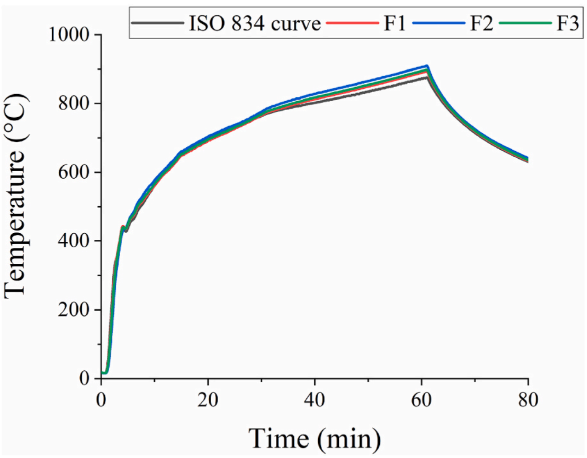

Fig. 4. ISO 834 standard fire curve and the furnace temperature curves for the thermocouples F1, F2 and F3 (the test was stopped after 60 min, and the cooling down was recorded for additional 20 min).

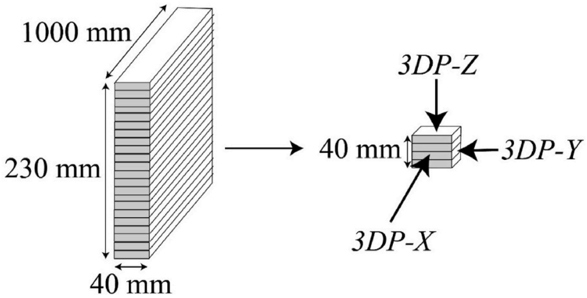

Fig. 5. Testing directions for structural adequacy (not to scale).

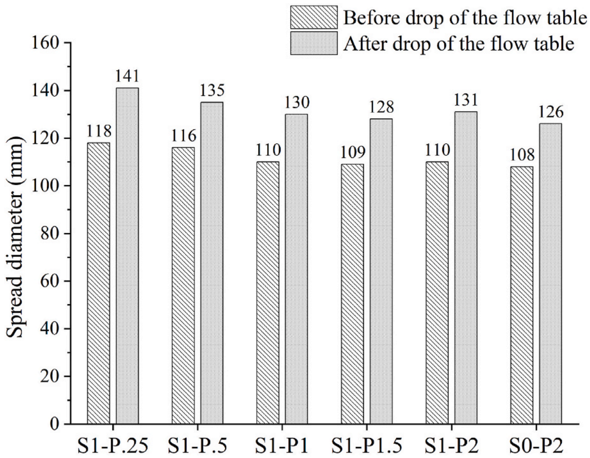

Fig. 6. Flow table average spread diameters of the fresh mixtures.

drop of the flow table – which was a desirable characteristic for the extrusion. The average spread diameters of the fresh mixtures after the drop of the flow table satisfy the printability region recommended in Tay et al. [48]. As expected, the workability was slightly reduced with the increase of the polymer fibers due to the interlocking effect of the fiber within the mixture. Additionally, the increase in the internal surface area per unit volume of the composite slightly increased the adsorption of the mix water. However, no significant workability difference was observed between the mixtures with polymer fiber volume fraction higher than 1 %.

4.2. Moisture content

Table 3 presents the moisture content of the panel specimens on the day of testing. The moisture content ranged between 3 % and 3.5 % for all specimens. Mold-cast panels showed a slightly higher moisture content than the 3D printed panels. This can be attributed to the evaporation via interlayers and early-age evaporation in the 3D printed specimens where the concrete is fully exposed. The effect of PP fiber volume fraction on the moisture content was found to be insignificant. During the fire test, the release of steam was observed in all specimens after 6–10 min from the start of the fire test. The steam intensified until 35 min and then slowly diminished after that.

4.3. Failure modes

Table 4 shows the failure modes of the specimens. When the PP fiber content was 0.25 % (S1-P.25 mixture), explosive spalling was observed in the mold-cast specimens, as can be seen in Fig. 7. An initial cracking was observed after 10 min, and the specimen was destroyed after 21 min. Meanwhile, the corresponding 3D-printed specimens did not show any spalling. However, delamination at the interlayers was observed in these specimens, as in Fig. 8. The length of the delamination along the interlayer ranged from 8 mm to 24

Table 3
Moisture content of the mold-cast and 3D printed specimens on the day of testing.

Mixtures	S1-P.25	S1-P.5	S1-P1	S1-P1.5	S1-P2	S0-P2
Mold-cast	3.3 %	3.1 %	3.3 %	3.2 %	3.5 %	3.4 %
3DCP	3.1 %	3.1 %	3 %	3 %	3.1 %	3.2 %

Table 4
Failure modes of mold-cast and 3D printed panel specimens.

	S1-P.25	S1-P.5	S1-P1	S1-P1.5	S1-P2	S0-P2
Mold-cast	Explosive spalling of large sections	Spalling of small pieces	Random and local spalling	No spalling	No spalling	No spalling
3DCP	Interlayer delamination and visible cracks	No spalling, No interlayer delamination	No spalling, No interlayer delamination	No spalling, No interlayer delamination	No spalling, No interlayer delamination	No spalling, No interlayer delamination

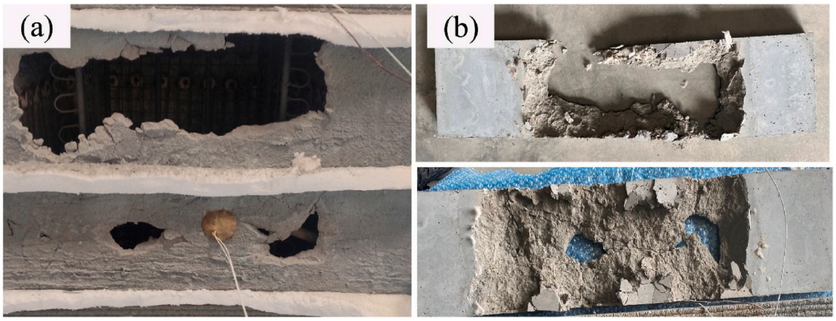

Fig. 7. Mold-cast specimens of S1-P.25 mixture following the fire test (a) unexposed surface (b) exposed surface.

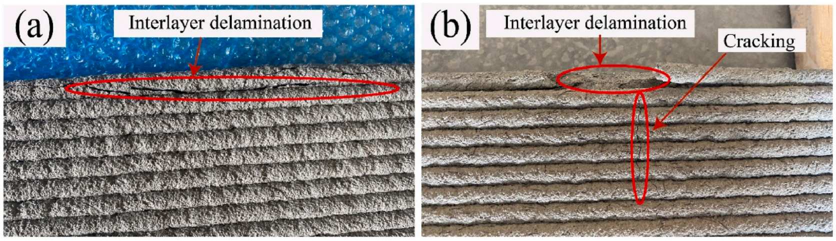

Fig. 8. 3D printed specimens of S1-P.25 mixture following the fire test (a) unexposed surface (b) exposed surface.

mm. The delamination was combined with cracks forming across the exposed surface, which can be attributed to the increased tensile stresses developed due to the thermal bowing of the specimens. The delamination of the interlayer was extended up to the unexposed surface. However, no cracks were observed in the unexposed surface, which can be attributed to the resistance of UHPFRC specimens to the compressive stresses in the unexposed surface due to thermal bowing and excessive drying. Figs. 9 and 10 present the exposed face of mold-cast and 3D printed specimens of the S1-P.5 mixture, respectively. When the fiber content was 0.5 %, no explosive spalling or interlayer delamination was observed in either mold-cast or 3D printed specimens. The S1-P.5 mixture was adopted to build a fire shelter using 3DCP method and the performance of the developed 3D printed UHPFRC and the application potential to build fire resistant structures are discussed by authors in a separate study [49]. However, small debris less than 10 mm fell off from the mold-cast panels, as shown in Fig. 9. This can be attributed to the lack of PP fibers in the UHPFRC system to sufficiently reduce the vapor pressure.

When the PP fiber volume content was 1 % (S1-P1 mixture), neither spalling nor interlayer delamination effects were observed in the 3D printed specimens. However, one spalling event was observed in one of the mold-cast specimens, as shown in Fig. 11. The spalling was about 20 mm wide and 5 mm in depth. The tensile cracks on the exposed surface were observed in both mold-cast and 3D printed specimens. This could potentially be due to thermal bowing, but it can be seen in the later discussion that it is unlikely to be the cause.

When the PP fiber content was more than 1 % (S1-P1.5, S1-P2, and S0-P2 mixtures), neither spalling nor interlayer delamination occurred in the specimens. Moreover, no surface cracks were observed in these specimens. (Figs. 12 and 13). The absence of surface cracks on the exposed surface when the fiber volume was more than 1 % indicates that the surface cracks are not due to thermal bowing but due to steam pressure build up.

The failure modes show how the panel eventually fails to provide the ability to maintain the fire separation. The increase in PP fiber content in the UHPFRC system improves the integrity of the panels. When the PP fiber volume fraction is less than 1 %, 3D printed panels showed better integrity than their mold-cast counterparts. When the PP fiber volume fraction is greater than 1 %, all mold-cast and 3D printed panels showed sufficient integrity up to 60 min.

It is notable that increasing the PP fiber content from 0.25 % to 0.5 % or more eliminated the interlayer delamination in the 3D printed specimens. The addition of PP fibers reduces the vapor pressure buildup inside the concrete and subsequently reduce the

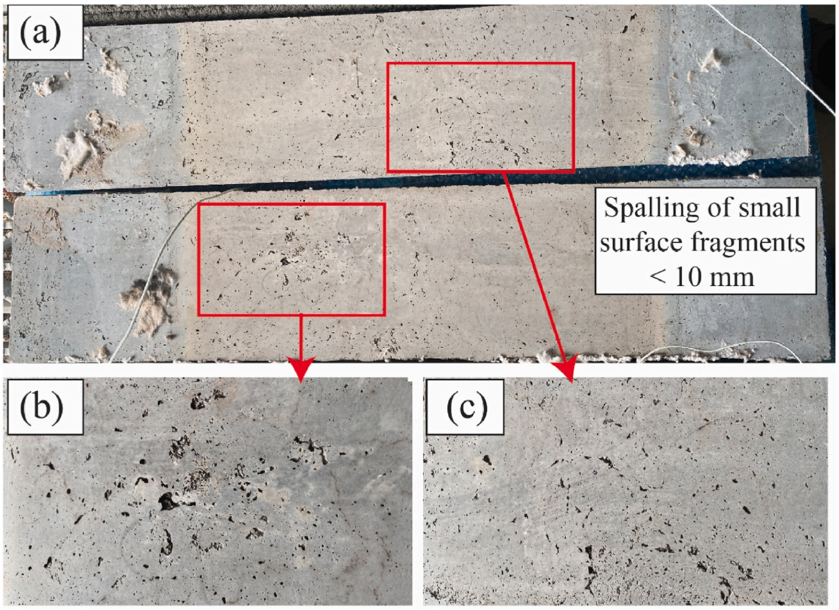

Fig. 9. (a) Exposed faces of mold-cast specimens of S1-P.5 mixture following the fire test (b) and (c) focused areas in the unexposed surfaces where the spalling of small fragments less than 10 mm occurred.

Fig. 10. Exposed face of 3D printed specimens of S1-P.5 mixture following the fire test [49].

damage in concrete. However, the interlayer zones in 3D printed specimens are naturally more porous and hence, are expected to have lower vapor pressure buildup compared to other sections of the printed concrete. Therefore, the effects of PP fiber on the interlayer delamination seem unclear.

4.4. Heat transfer

The heat transfer from the exposed face to the unexposed face of the panel specimens was measured from the thermocouple readings attached to the unexposed face of the specimens. At the beginning of the fire tests, the thermocouple measurements of the specimens were the same as the ambient temperature (20 ± 3 °C). During the fire tests, the measurements were recorded at 5 Hz at the surface and the interlayer (for 3D printed specimens only) of the unexposed faces. The time-temperature curves gathered from the thermocouple readings of the panel specimens are shown in Fig. 14. The temperatures measured at the surface of mold-cast and the 3D-printed specimens were comparable for all the fiber systems employed in the mixtures. This indicates that the ultra-dense low porosity microstructure of UHPFRC is identical in the mold-cast and 3D printed specimens. However, the temperatures measured at the interlayer of the unexposed faces of 3D printed specimens were significantly higher than the temperatures measured at the surface of the same specimens. In the specimens tested for up to 25 min (S1-P.25 and S1-P.5 mixtures), the interlayer temperature of the unexposed face reached between 225 °C and 275 °C at the end of the test, while the surface temperature of the unexposed face was below 150 °C. In the specimens tested for up to 60 min (S1-P1, S1-P.15, S1-P2, and S0-P2 mixtures), the interlayer temperatures of the unexposed face at the end of the test were 100–150 °C higher than the surface temperature of the printed panel specimens. For example, in the S1-P1 sample, 350 °C surface temperature was reached in the mold-cast and 3D printed specimens between 55 and 60 min, whereas the same temperature was reached at the interlayer of the same 3D printed specimens between 35 and 40 min. This observation was always true for all the samples, except for the initial 2–3 min of the fire test. This indicates a faster rate of heat transfer via the interlayers of the printed specimens. This phenomenon was also predicted by Cicione et al. [36] based on the laboratory fire

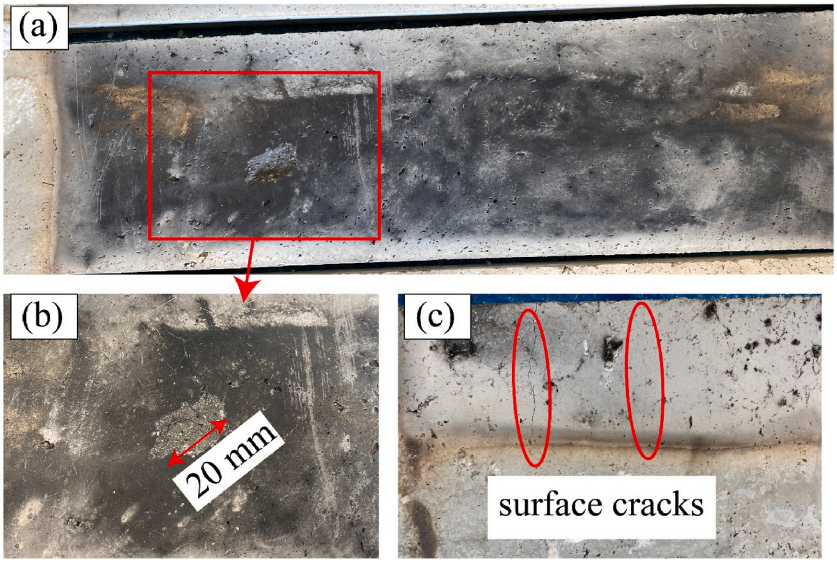

Fig. 11. (a) Exposed face of mold-cast specimens of S1-P1 mixture following the fire test (b) focused region where a localized 20 mm wide spalling occurred (c) surface cracks on observed on the exposed surface.

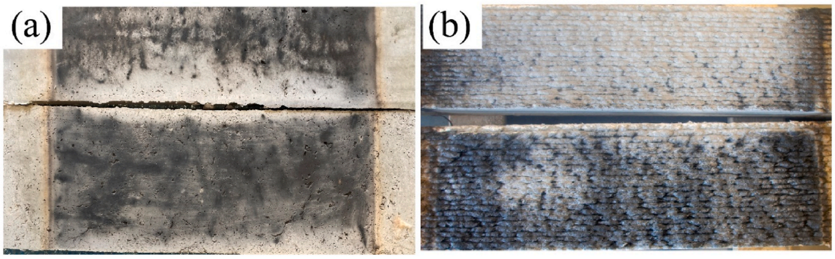

Fig. 12. Exposed faces of panel specimens S0-P2 mixture following the fire test (a) mold-cast specimens (b) 3D printed specimens. No visible damages were observed.

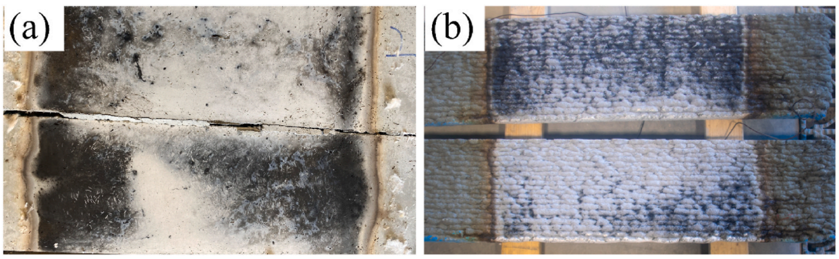

Fig. 13. Exposed faces of panel specimens S1-P2 mixture following the fire test (a) mold-cast specimens (b) 3D printed specimens. No visible damages were observed.

tests conducted on 3D printed normal strength concretes, though their experimental results did not provide unambiguous evidence for the prediction. Based on the experimental data collected in this study, it can be confirmed that the rate of heat transfer via the interlayer is faster than that via the surface of the concrete.

Previous studies reported that the interlayer zones in the 3D printed specimens were porous due to their undulating surfaces, which also led to weak bond strengths [50–52]. While the porous microstructure improves the thermal insulation of the concrete by reducing thermal conductivity, the test data indicates otherwise. It can be argued that the interlayer zones have lower thermal capacity than the rest of the concrete, which may slightly delay the heat transfer via the interlayers [53]. However, this may not hold accurate for porous interlayer microstructure since the heat conduction via a solid medium is several folds higher than that via air/pores. Therefore, it appears there are 'gaps' present in the interlayer zones of the 3D printed specimens that allow for heat transfer. These gaps effectively

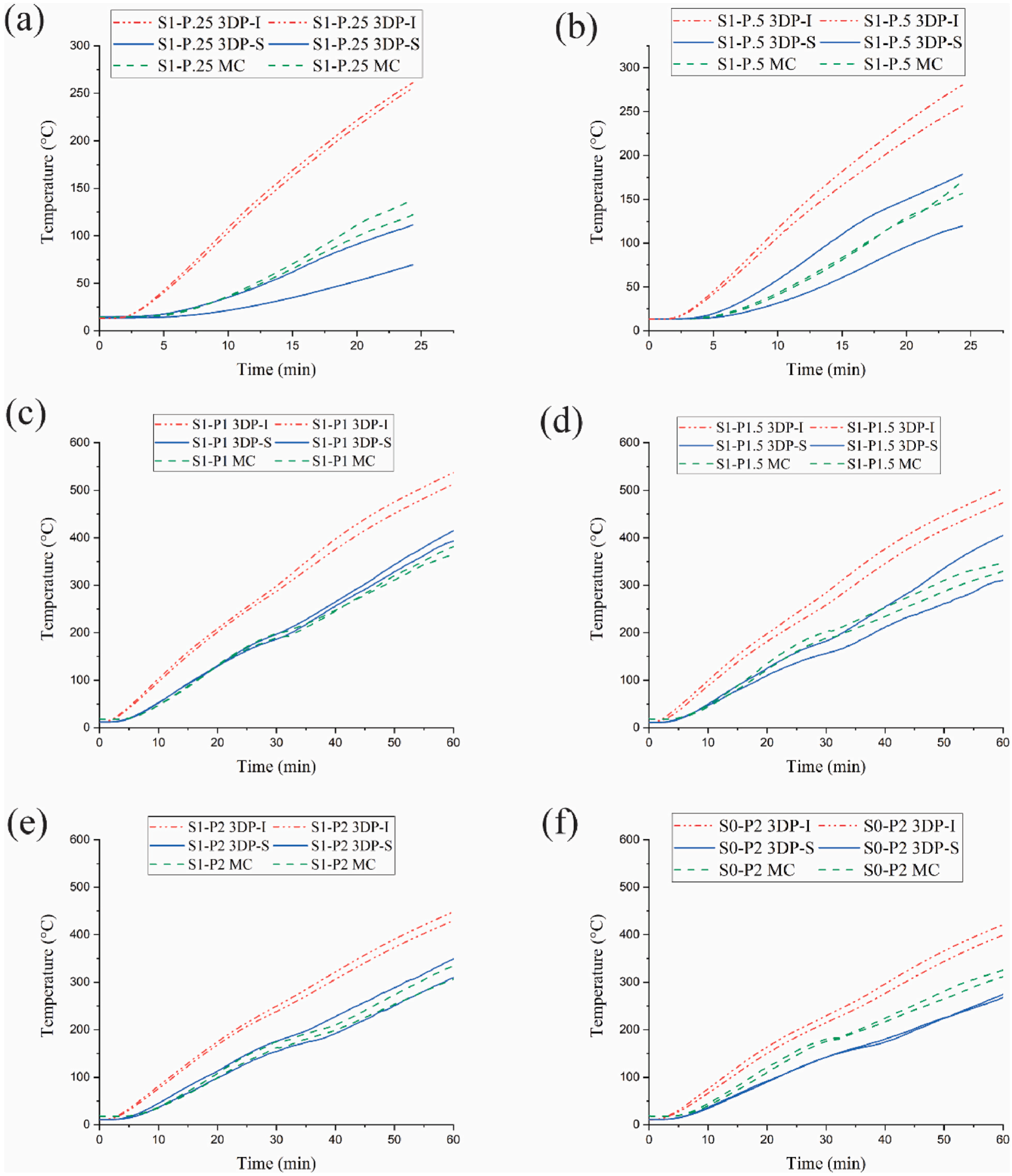

Fig. 14. Temperature measured at the unexposed face of the specimens (a) S1-P.25 (b) S1-P.5 (c) S1-P1 (d) S1-P1.5 (e) S1-P2 (f) S0-P2 (MC denotes the mold-cast panels, 3DP-I denotes the interface of the 3D printed panels, and 3DP-S denotes the surface of the 3D printed panels).

reduce the thickness of the interlayer zones so that the heat transfers via a combination of convection, radiation and conduction to the unexposed interlayer zones. Since the heat transfer via convection and radiation is faster than conduction, the interlayer zones allow for the rapid transfer of heat compared to the concrete surfaces. To mitigate the rapid heat transfer via the interlayers, the adjacent layers of the 3D printed concrete must be wet pressed while printing so that the gap formations are prevented. This means that the top and bottom layers should be sufficiently moist while printing to improve the fire performance of the 3D printed concrete specimens

[50]. Further, incorporating polymer-modified mortars improves interlaminar bonding, thereby reducing the pores. Additionally, varying the printing time interval also improves the interlayer bonding and thereby reduce the heat transfer through the interlayer [36].

Among the specimens exposed to 60 min of fire test, the unexposed surface temperature of the panel specimens was in the order: S1-P1 > S1-P1.5 > S1-P2 > S0-P2. This observation was true for 3D printed and mold-cast specimens. Moreover, the unexposed interlayer zone temperatures of the 3D printed panel specimens followed the same order. This indicates that the addition of PP fibers reduces the rate of heat transfer via conduction across the specimens. The latent heat for phase change expended on the melting of the PP fibers reduces the rate of heat transfer, which in return increases the insulation and fire resistance capabilities of the panel specimens. Between S1-P2 and S0-P2 mixtures, the difference in the rate of heat transfer is low, indicating the minimal contribution of the steel fibers in the insulation of the panel specimens.

4.5. Minimum insulation requirements

Fig. 15 shows the thermal insulation of the panel specimens, measured as the time taken for the average temperature of the unexposed surface of the specimens to exceed the room temperature by 180 °C [46]. The mixtures S1-P.25 and S1-P.5 were not reported, as the fire test was stopped due to spalling before the insulation failure criteria discussed in Section 3.3 was met. Among the rest of the mixtures, the insulation resistance periods at the interfaces of the 3D printed panels range between 20 and 25 min, while the surface of the 3D printed panels and the mold-cast panels showed more than 30 min of insulation resistance. It must be noted that these time periods are lower than those recommended in Ref. [25]. However, the panel sections were only 40 mm in thickness, which was also lower than the recommended thickness (>100 mm). As we discussed earlier, the interfaces of the 3D printed specimens transferred the heat rapidly due to their porous microstructure, leading to low insulation resistance. In each mixture, the surface of the 3D printed specimens and the mold-cast specimens showed comparable resistance times. The insulation resistance time of both mold-cast and 3D printed specimens increased with the addition of PP fibers.

4.6. Thermal bowing

Thermal bowing was observed in all specimens during the fire test. The deflection was the highest at the central part of the specimen, bending inwards to the furnace, as illustrated in Fig. 16.

The mid-span deflections of the specimens were measured following the cooling period. The thermal bowing effect can be theoretically presented in the following manner. The out-of-plane displacement (u) at a distance x along the span l of the specimen can be given as in Equation (3). The maximum displacement at the mid-span can be calculated when $x = \frac{l}{2}$.

$$u(x) = \varnothing . \frac{x(l-x)}{2} \tag{3}$$

where $\varnothing$ is the curvature of the bowing effect and can be derived from Equation (4). ϵ is the thermal strain from the bowing effect.

$$\varnothing = \frac{\epsilon}{t} \tag{4}$$

Where t is the thickness of the panel (or the width of the layer in the 3D printed specimens) and equals to 40 mm.

At ambient conditions, the thermal conductivity of concrete mixtures can be assumed constant [19,54]. However, the thermal conductivity of concrete reduces at high temperatures such as those achieved during fire tests [55]. When siliceous aggregates are used, the value of ϵ with reference to the length at 20 °C can be derived from Equation (5) [56].

$$\epsilon = -1.8 \times 10^{-4} + 9 \times 10^{-6}\theta + 2.3 \times 10^{-11}\theta^3 \tag{5}$$

where θ is the difference between the concrete temperatures at the exposed and unexposed faces. For 3D printed specimens, the value of θ is not similar at the interlayer and the surfaces, as discussed earlier. In addition, the θ at the interlayer appears to be a combined effect of conduction and radiation, whereas the θ at the surface is solely attributed to conduction. Therefore, an additional coefficient, interface to surface heat transfer ratio, β was introduced (as in Equation (6)) to differentiate the heat transfers via surface zones and the interlayer zones.

$$\theta = \beta(\theta_u - \theta_i) + (1-\beta)(\theta_u - \theta_s) \tag{6}$$

where θ_u, θ_i, θ_s represents the concrete temperatures at the unexposed face, interlayer zone, and the surface zone, respectively. It must be noted that β may not be a constant throughout the entire time period of the fire test, as the rate of heat transfer across the specimen varies. However, for simplicity, we can evaluate β values of the panels at the end of the fire test (i.e., 60 min) for the maximum deflection at the mid-span. In the mold-cast specimens, β can be assumed to be zero. The maximum out-of-plane displacement at the mid-span, the corresponding thermal strain, and the calculated β values of the 3D printed panels were given in Table 5.

From Table 5, we can note that the thermal bowing of 3DP-UHPFRC panels increased with the increase in PP fiber volume fraction. The high amount of PP fibers reduces the heat transfer, thus increasing the temperature differences between the exposed and unexposed faces, leading to high thermal strains and subsequently high bowing. Meanwhile, the β values of the 3D-printed panels range

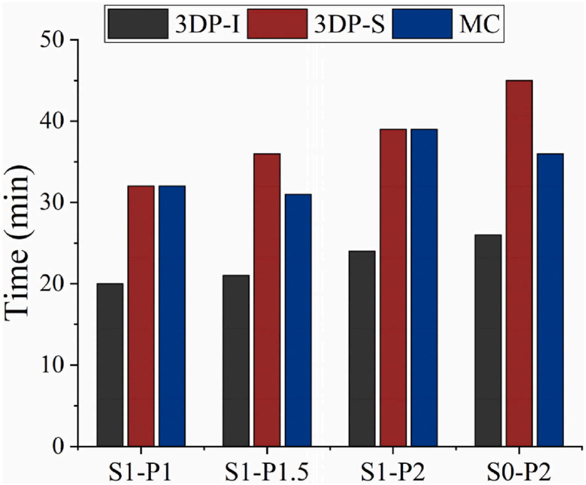

Fig. 15. Insulation resistance of the panels (3DP-I denotes the interface of the 3D printed panels, 3DP-S denotes the surface of the 3D printed panels and MC denotes the mold-cast panels).

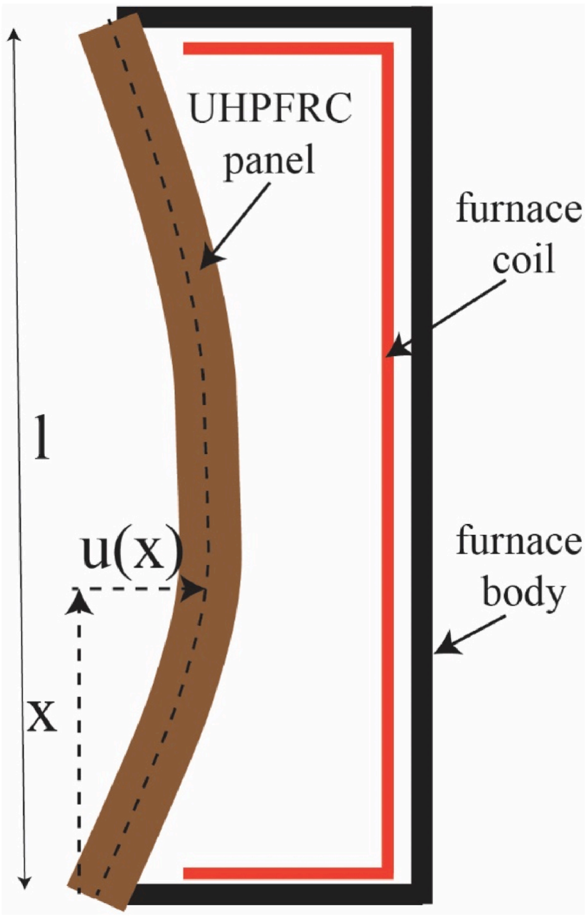

Fig. 16. Thermal bowing of UHPFRC panels (top view, not to scale).

between 0.1 and 0.16. For a 10 mm layer thickness (which was used in this study), the effect of the interlayer on the heat transfer accounted for 1 mm and 1.6 mm of the surface. It must be noted that the β values did not show any meaningful correlation with the volume fraction of PP fibers in the composite.

Table 5
Thermal bowing of 3D printed UHPFRC panels.

	S1-P1		S1-P1.5		S1-P2		S0-P2	
	3DP-1	3DP-2	3DP-1	3DP-2	3DP-1	3DP-2	3DP-1	3DP-2
Displacement (mm) - measured	7.7	7.4	7.7	10.4	9.2	10.5	11.7	11.8
Thermal strain (10^{-6}) -calculated	6844	6578	6844	9244	8178	9333	10400	10489
β - calculated	0.14	0.11	0.12	0.10	0.12	0.13	0.16	0.15

For the cracking to occur, the thermal strains should exceed the tensile cracking strain (ϵ_{cr}) of the composite, as in Equation (7).

$$\epsilon > \epsilon_{cr} \tag{7}$$

It must be noted that the restrained thermal strains were measured after the cooling down of the specimens, which would be smaller than what occurred during the maximum thermal bowing during the fire test. However, we can argue that the thermal strains at the maximum deflection could be higher than the values presented in Table 5, hence the probability of tensile cracking due to thermal bowing is higher when the conditions given in Equation (7) are met.

4.7. Structural integrity

The structural integrity of the panel members was evaluated based on the residual compressive strength of the mixtures following the fire test. The mean compressive strength values of the mold-cast and 3D printed specimens before and after the fire tests are given in Fig. 17. Before the fire test, the specimens showed mean compressive strength values in the range of 105–155 MPa. This was slightly lower than those achieved in the base mixture (i.e., without any PP fibers) discussed elsewhere (3DP-X – 152.5 MPa, 3DP-Y – 133.7 MPa, 3DP-Z – 140.7 MPa, Mold-cast – 151.2 MPa) [40]. From Fig. 17, it can be seen that the addition of PP fibers reduced the mean compressive strength values of the specimens, in both mold-cast and 3D printed specimens. When the steel fibers were completely replaced with 2 % of PP fibers (S0-P2 mixture), the mean compressive strength values before the fire tests were reduced by 20 % in mold-cast specimens and 11–15 % in 3D printed specimens, depending on the testing direction. In the mixtures with hybrid steel-PP

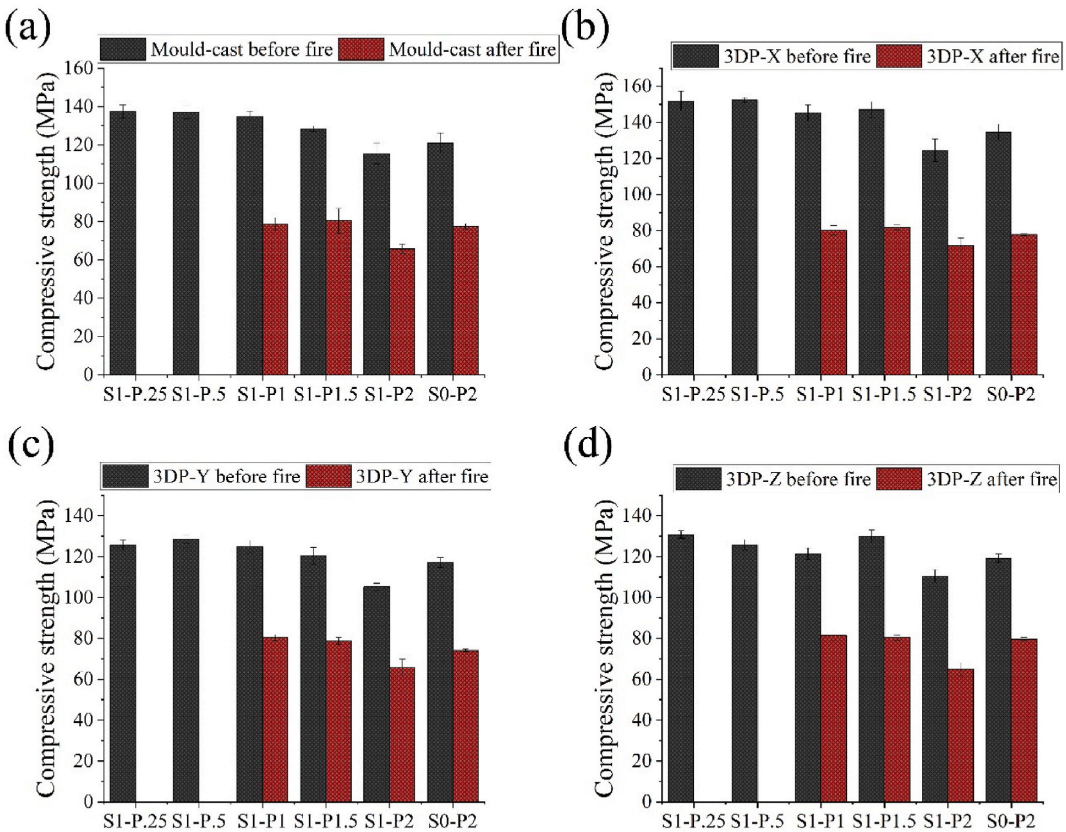

Fig. 17. Compressive strength of UHPFRC mixtures before and after the fire test (a) mold-cast specimens (b) 3DP-X specimens (c) 3DP-Y specimens (d) 3DP-Z specimens.

fiber systems, when the PP fibers were increased from 0.25 % (S1-P.25 mixture) to 2 % volume fraction (S1-P2 mixture), the mean compressive strength values before the fire tests were reduced by 16 % in the mold-cast specimens and 15–18 % in the 3D printed specimens, depending on the testing direction. The addition of PP fibers adversely influences the particle packing density of the UHPFRC, thereby leading to a porous microstructure compared to the base mixture design [57].

The residual compressive strength test values of S1-P.25 and S1-P.5 mixtures were not tested since those panel specimens failed due to explosive spalling, interlayer delamination, or spalling of small debris during the fire test, thereby causing the termination of the fire test prematurely. Among the rest of the mixtures, the residual compressive strength values (i.e., after the fire tests) of the mold-cast and 3D printed specimens retained between 55 % and 68 % of the mean compressive strength values of the mixtures before the fire tests. The strength reduction was caused by the loss of bound water and the decomposition of the portlandite and the carbonates in the microstructure of the specimens [58,59]. The residual compressive strength values of S1-P1, S1-P1.5, and S0-P2 mixtures were relatively comparable while the S1-P2 mixture showed the lowest residual compressive strength in both mold-cast and 3D printed specimens. However, the differences in the residual compressive strength are negligible compared to the loss of compressive strength from the fire tests.

The anisotropy indices of these specimens before and after the fire tests were calculated using Equation (2) separately and were shown in Fig. 18. The anisotropy indices were lower in the specimens after the fire test compared to those observed before the fire test. This can be attributed to the forming of random porous microstructure due to the decomposition of portlandite and carbonates, and the melting of polymeric fibers [32,60]. This random porous microstructure weakens the mechanical behavior of the 3D printed specimens, thereby eliminating the significance of interlayer zones. In addition, the fire test event was by itself non-homogenous, as the heat transferred from the exposed face to the unexposed face of the specimens – leading to inconsistent damages across the thickness of the specimens. As these effects create localized failures in the specimens under the compressive loading, the effects of testing directions become insignificant.

5. Conclusions

This study investigates the fire response of mold-cast and 3D-printed panels made with the developed UHPFRC with different hybrid fiber systems (steel and PP fibers). The panels were subjected to the ISO 834 standard fire curve test for up to 60 min, and their structural adequacy, integrity, and insulation were measured. The following conclusions can be drawn from the study.

(a) The failure mode of 3D-printed panels was predominantly interlayer delamination, compared to the spalling of mold-cast specimens. When the PP fibers were 0.25 %, the mold-cast specimens failed in explosive spalling (<25 min), while the 3D printed specimens did not spall due to the presence of interlayers, thereby showing better structural integrity.
(b) Spalling was observed in the mold-cast specimens when PP fiber volume is less than 1 %. However, localized and isolated spalling was observed at 1 % PP fiber volume fraction. Furthermore, no spalling was observed when the PP fiber content was above 1 % volume fraction. In the 3D printed specimens, neither interlayer delamination nor spalling was observed when the PP fiber content was above 0.5 % volume fraction.
(c) The heat transfer via the interlayers was significantly higher than that via the surface of the specimens. This rapid heat transfer worsens the minimum insulation requirements of 3D printed panels compared to the mold-cast specimens. It appears there are gaps at the interlayers that reduce the effective thickness of the panels and facilitate heat transfer. Apart from the interlayers, the heat transfer of the 3D printed specimens is comparable to the heat transfer in the mold-cast specimens.

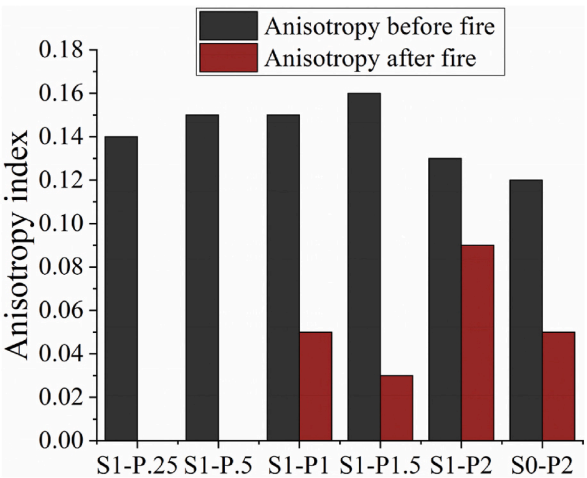

Fig. 18. Anisotropy index of UHPFRC mixtures.

(d) The addition of PP fibers slightly reduces the mean compressive strength of the mold-cast and 3D printed specimens before the fire tests. The residual compressive strength (i.e., after the fire tests) of the mold-cast and 3D printed specimens retained between 55 % and 68 % of the mean compressive strength values before the fire tests. The reduction is due to the decomposing of portlandite and carbonates in UHPFRC's microstructure.
(e) The anisotropy index of the residual compressive strength values of 3D printed specimens withered away following the fire tests. This can be attributed to the inconsistency in the damages to the microstructure as the heat transferred from one direction to the other, thereby eliminating the anisotropic effects of 3D printing.

The current study focuses on the behavior of 3D printed UHPFRC panels subjected to ISO standard fire curve experimentally. However, further investigation on the thermal stress-strain model can provide more insight to carry out detailed numerical modelling of 3D printed UHPFRC panels subjected to various fire exposures.

CRediT authorship contribution statement

Arun R. Arunothayan: Writing – original draft, Validation, Project administration, Investigation, Formal analysis, Data curation, Conceptualization. **Akilesh Ramesh:** Writing – review & editing, Methodology, Investigation, Formal analysis, Data curation. **Jay G. Sanjayan:** Writing – review & editing, Validation, Supervision, Resources, Project administration, Investigation, Funding acquisition, Conceptualization.

Declaration of competing interest

The authors declare that they have no known competing financial interests or personal relationships that could have appeared to influence the work reported in this paper.

Acknowledgments

The authors greatly acknowledge the support provided by the Australian Research Council Discovery Project grant DP170103521. The authors are also thankful to the staff of the Digital Construction Laboratory and Smart Structures Laboratory at Swinburne University of Technology.

Data availability

Data will be made available on request.

References

[1] T. Wangler, N. Roussel, F.P. Bos, T.A. Salet, R.J. Flatt, Digital concrete: a review, Cement Concr. Res. 123 (2019) 105780.
[2] V. Mechtcherine, F.P. Bos, A. Perrot, W.L. da Silva, V.N. Nerella, S. Fataei, R.J. Wolfs, M. Sonebi, N. Roussel, Extrusion-based additive manufacturing with cement-based materials–production steps, processes, and their underlying physics: a review, Cement Concr. Res. 132 (2020) 106037.
[3] S. Muthukrishnan, S. Ramakrishnan, J. Sanjayan, Technologies for improving buildability in 3D concrete printing, Cem. Concr. Compos. 122 (2021) 104144.
[4] T. Marchment, J. Sanjayan, Reinforcement method for 3D concrete printing using paste-coated bar penetrations, Autom. ConStruct. 127 (2021) 103694.
[5] A. Ramesh, P. Rajeev, J. Sanjayan, Bond-slip behaviour of textile-reinforcement in 3D printed concrete, J. Build. Eng. 86 (2024) 108873.
[6] A. Ramesh, P. Rajeev, J. Sanjayan, V. Mechtcherine, In-process textile reinforcement method for 3D concrete printing and its structural performance, Eng. Struct. 314 (2024) 118337.
[7] A.R. Arunothayan, B. Nematollahi, R. Ranade, S.H. Bong, J. Sanjayan, Development of 3D-printable ultra-high performance fiber-reinforced concrete for digital construction, Construct. Build. Mater. 257 (2020) 119546.
[8] A.R. Arunothayan, B. Nematollahi, R. Ranade, K.H. Khayat, J.G. Sanjayan, Digital fabrication of eco-friendly ultra-high performance fiber-reinforced concrete, Cem. Concr. Compos. 125 (2022) 104281.
[9] R. Arunothayan, Investigation of Ultra-high Performance Concrete for 3D Construction Printing (Doctoral Dissertation, Swinburne University of Technology), 2023.
[10] A. Ramesh, Investigation of Textile Reinforcement for 3D Concrete Printing Applications (Doctoral Dissertation, Swinburne), 2024.
[11] C. Gosselin, r. Duballet, p. Roux, N. Gaudillière, J. Dirrenberger, P. Morel, P., Large-scale 3D printing of ultra-high performance concrete–a new processing route for architects and builders, Mater. Des. 100 (2016) 102–109.
[12] Y. Yao, J. Zhang, Y. Sun, Y. Pi, J. Wang, C. Lu, Mechanical properties and failure mechanism of 3D printing ultra-high performance concrete, Construct. Build. Mater. 447 (2024) 138108.
[13] D. Heinz, F. Dehn, L. Urbonas, Fire resistance of ultra high performance concrete (UHPC)-Testing of laboratory samples and columns under load. International Symposium on Ultra High Performance Concrete, Kassel Germany, 2004, pp. 703–715.
[14] M. Siemon, J. Zehfuß, Experimental and numerical analysis of ultra high performance concrete (UHPC) members in case of fire, Appl. Struct. Fire Eng. (2015).
[15] G.A. Khoury, Effect of fire on concrete and concrete structures, Prog. Struct. Eng. Mater. 2 (2000) 429–447.
[16] X. Hou, P. Ren, Q. Rong, W. Zheng, Y. Zhan, Comparative fire behavior of reinforced RPC and NSC simply supported beams, Eng. Struct. 185 (2019) 122–140.
[17] S. Ahmad, M. Rasul, S.K. Adekunle, S.U. Al-Dulaijan, M. Maslehuddin, S.I. Ali, Mechanical properties of steel fiber-reinforced UHPC mixtures exposed to elevated temperature: effects of exposure duration and fiber content, Compos. B Eng. 168 (2019) 291–301.
[18] S. Banerji, V. Kodur, R. Solhmirzaei, Experimental behavior of ultra high performance fiber reinforced concrete beams under fire conditions, Eng. Struct. 208 (2020) 110316.
[19] V. Kodur, Properties of concrete at elevated temperatures, Int. Sch. Res. Notices (2014).
[20] H. Qin, J. Yang, K. Yan, J.H. Doh, K. Wang, X. Zhang, Experimental research on the spalling behaviour of ultra-high performance concrete under fire conditions, Construct. Build. Mater. 303 (2021) 124464.

[21] J. Zhao, J.J. Zheng, G.F. Peng, K. van Breugel, A meso-level investigation into the explosive spalling mechanism of high-performance concrete under fire exposure, Cement Concr. Res. 65 (2014) 64–75.
[22] Y. Li, P. Du, K.H. Tan, Fire resistance of ultra-high performance concrete columns subjected to axial and eccentric loading, Eng. Struct. 248 (2021) 113158.
[23] X. Liang, C. Wu, Y. Yang, Z. Li, Z. Experimental study on ultra-high performance concrete with high fire resistance under simultaneous effect of elevated temperature and impact loading, Cem. Con. Compos. 98 (2019) 29–38.
[24] ISO 834-1, Fire-resistance Tests Elements of Building Construction Part 1: General Requirements, International Organization for Standardization, 1999, p. 30.
[25] AS 1530.4, Methods for Fire Tests on Building Materials, Components and Structures, Part 4: Fire-Resistance Tests for Elements of Construction, Standards Australia, 2014, p. 154.
[26] P. Weerasinghe, K. Nguyen, P. Mendis, M. Guerrieri, Large-scale experiment on the behaviour of concrete flat slabs subjected to standard fire, J. Build. Eng. 30 (2020) 101255.
[27] G. Wang, D. Barber, P. Johnson, M.C. Hui, Fire safety provisions for aged concrete building structures, Procedia Eng. 62 (2013) 629–638.
[28] K. Dhasindrakrishna, S. Ramakrishnan, K. Pasupathy, J. Sanjayan, Synthesis and performance of intumescent alkali-activated rice husk ash for fire-resistant applications, J. Build. Eng. (2022) 104281.
[29] L. Li, L. Shi, Q. Wang, Y. Liu, J. Dong, H. Zhang, G. Zhang, A review on the recovery of fire-damaged concrete with post-fire-curing, Construct. Build. Mater. 237 (2020) 117564.
[30] Y. Zhu, H. Hussein, A. Kumar, G. Chen, A review: material and structural properties of UHPC at elevated temperatures or fire conditions, Cem. Concr. Compos. 123 (2021) 104212.
[31] J.H. Lee, Y.S. Sohn, S.H. Lee, Fire resistance of hybrid fibre-reinforced, ultra-high-strength concrete columns with compressive strength from 120 to 200 MPa, Mag. Concr. Res. 64 (6) (2012) 539–550.
[32] C. Kahanji, F. Ali, A. Nadjai, Explosive spalling of ultra-high performance fibre reinforced concrete beams under fire, J. Struct. Fire Eng. 7 (2016) 328–348.
[33] G. Choe, G. Kim, N. Gucunski, S. Lee, Evaluation of the mechanical properties of 200 MPa ultra-high-strength concrete at elevated temperatures and residual strength of column, Construct. Build. Mater. 86 (2015) 159–168.
[34] X. Cai, L.R. Taerwe, Y. Yuan, Hysteretic behavior of UHPC beam-column joints after fire exposure, Fire Saf. J. 117 (2020) 102987.
[35] K. Liu, C. Wu, X. Li, M. Tao, J. Li, J. Liu, S. Xu, Fire damaged ultra-high performance concrete (UHPC) under coupled axial static and impact loading, Cem. Concr. Compos. 126 (2022) 104340.
[36] A. Cicione, J. Kruger, R.S. Walls, G. Van Zijl, An experimental study of the behavior of 3D printed concrete at elevated temperatures, Fire Saf. J. 120 (2021) 103075.
[37] T. Suntharalingam, P. Gatheeshgar, I. Upasiri, K. Poologanathan, B. Nagaratnam, M. Corradi, D. Nuwanthika, Fire performance of innovative 3D printed concrete composite wall panels–A Numerical Study, Case Stud. Constr. Mater. 15 (2021) e00586.
[38] T. Suntharalingam, I. Upasiri, P. Gatheeshgar, K. Poologanathan, B. Nagaratnam, H. Rajanayagam, S. Navaratnam, Fire resistance of 3D printed concrete composite wall panels exposed to various fire scenarios, J. Struct. Fire Eng. 12 (2021) 377–409.
[39] A. Ramesh, S. Navaratnam, P. Rajeev, J. Sanjayan, Thermal performance and life cycle analysis of 3D printed concrete wall building, Energy Build. 320 (2024) 114604.
[40] A.R. Arunothayan, B. Nematollahi, R. Ranade, S.H. Bong, J.G. Sanjayan, K.H. Khayat, Fiber orientation effects on ultra-high performance concrete formed by 3D printing, Cement Concr. Res. 143 (2021) 106384.
[41] K. Wille, A.E. Naaman, G.J. Parra-Montesinos, Ultra-high performance concrete with compressive strength exceeding 150 MPa (22 ksi): a simpler way, ACI Mater. J. 108 (2011).
[42] A.R. Arunothayan, J.G. Sanjayan, Elevated temperature effects on 3D printed ultra-high performance concrete, Construct. Build. Mater. 367 (2023) 130241.
[43] A.R. Arunothayan, B. Nematollahi, K.H. Khayat, A. Ramesh, J.G. Sanjayan, Rheological characterization of ultra-high performance concrete for 3D printing, Cem. Concr. Compos. (2022) 104854.
[44] ASTM C1437, Standard Test Method for Flow of Hydraulic Cement Mortar, ASTM International, 2007.
[45] E. Negahban, A. Bagheri, A. Al-Dujaili, J. Sanjayan, Insulation failure of lightweight composite sandwich panels exposed to flame, Fire Mater. 44 (2020) 943–952.
[46] Q. Nguyen, T. Ngo, P. Tran, P. Mendis, L. Aye, S.K. Baduge, Fire resistance of a prefabricated bushfire bunker using aerated concrete panels, Construct. Build. Mater. 174 (2018) 410–420.
[47] G. Ma, Z. Li, L. Wang, F. Wang, J. Sanjayan, Mechanical anisotropy of aligned fiber reinforced composite for extrusion-based 3D printing, Construct. Build. Mater. 202 (2019) 770–783.
[48] Y.W.D. Tay, Y. Qian, M.J. Tan, Printability region for 3D concrete printing using slump and slump flow test, Compos. B Eng. (2019) 106968.
[49] A.R. Arunothayan, J. Sanjayan, M. Surti, F. Schneider, 3D Printing of Fire Shelter Using Ultra-High Performance Concrete. In International Interactive Symposium on Ultra-High Performance Concrete 2023. (Vol. vol. 3, No. 1). Iowa State University Digital Press. https://doi.org/10.21838/uhpc.16650.
[50] J.G. Sanjayan, B. Nematollahi, M. Xia, T. Marchment, Effect of surface moisture on inter-layer strength of 3D printed concrete, Construct. Build. Mater. 172 (2018) 468–475.
[51] J. Van Der Putten, M. Deprez, V. Cnudde, G. De Schutter, K. Van Tittelboom, Microstructural characterization of 3D printed cementitious materials, Mater 12 (2019) 2993.
[52] V.N. Nerella, S. Hempel, V. Mechtcherine, Effects of layer-interface properties on mechanical performance of concrete elements produced by extrusion-based 3D-printing, Construct. Build. Mater. 205 (2019) 586–601.
[53] S. Ramakrishnan, S. Muthukrishnan, J. Sanjayan, K. Pasupathy, Concrete 3D printing of lightweight elements using hollow-core extrusion of filaments, Cem. Concr. Compos. 123 (2021) 104220.
[54] K.-Y. Shin, S.-B. Kim, J.-H. Kim, M. Chung, P.-S. Jung, Thermo-physical properties and transient heat transfer of concrete at elevated temperatures, Nucl. Eng. Des. 212 (2002) 233–241.
[55] W. Khaliq, Performance Characterization of High Performance Concretes under Fire Conditions, Michigan State University, 2012. PhD Thesis.
[56] BS EN1992-1-1:2004 Eurocode 2: Design of Concrete Structures, General rules and rules for buildings, 2004.
[57] S. Sanchayan, S.J. Foster, High temperature behaviour of hybrid steel–PVA fibre reinforced reactive powder concrete, Mater. Struct. 49 (2016) 769–782.
[58] G.-F. Peng, Y.-R. Kang, Y.-Z. Huang, X.-P. Liu, Q. Chen, Experimental research on fire resistance of reactive powder concrete, Adv. Mater. Sci. 2012 (2012) 860303.
[59] X. Liang, C. Wu, Y. Su, Z. Chen, Z. Li, Development of ultra-high performance concrete with high fire resistance, Construct. Build. Mater. 179 (2018) 400–412.
[60] V. Kodur, S. Banerji, R. Solhmirzaei, Effect of temperature on thermal properties of ultrahigh-performance concrete, J. Mater. Civ. Eng. 32 (2020) 04020210.